CHAPTER 4

RESULTS AND DISCUSSION

This chapter shows the results and discussions of the NiO films sparked on flexible Cr/Au coated PET substrates and Ni foams. The structures and morphologies of the NiO nanoparticles and NiO films were examined using SEM, EDS, XRD, TEM, UV-vis, XPS, BET, AFM and Raman. Moreover, the electrochemical energy-storage performances of the NiO films were evaluated by CV, GCD and EIS.

4.1 Results and discussion of the NiO films sparked on flexible Cr/Au coated PET substrates

4.1.1 Material characterization

1) SEM results of the sparked NiO film

Figure 4.1 shows typical top-view and cross-sectional-view SEM images of a sparked NiO film. From the top-view image (Figure 4.1 (a)-(b)), it can be seen that the film comprises very fine nanometer-sized particles loosely agglomerated into porous foam-like network. In addition, it contains a large number of pores with various sizes ranging from a few to hundreds nanometers. The cross-sectional view image (Figure 4.1 (c)) demonstrates that the NiO layer prepared by sparking method is a homogenous and regular film with high surface roughness. The average layer thickness is estimated to be ~2.6 ± 0.27 μm. The result confirms that a uniform film of loosely packed nanoparticles with microns in thickness can be effectively produced by the specially designed sparking system with electrode array and two-dimensional scanning.

2) AFM results of the NiO films sparked on flexible Cr/Au coated PET substrates

The surface topography of the sparked NiO film was examined and compared with that of Cr-Au on PET substrate as illustrated in Figure 4.2. It is seen that the NiO sparked film displays a bumpy surface comprising agglomerated secondary

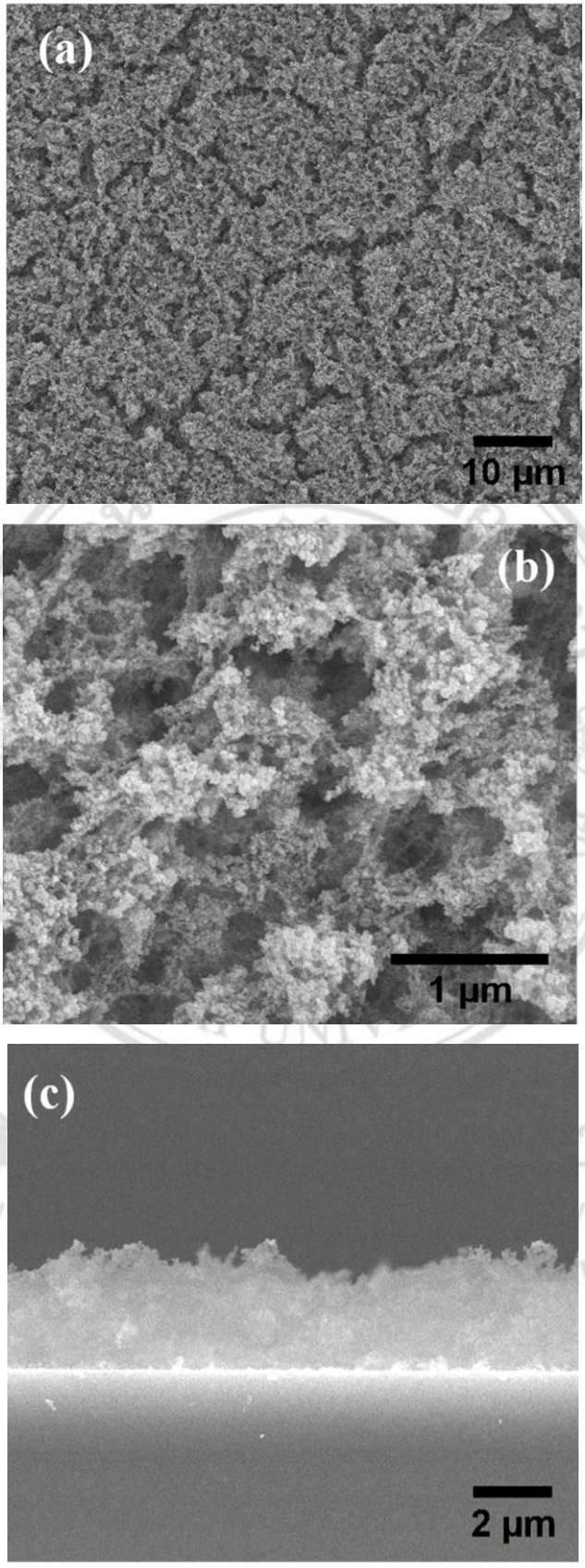

Figure 4.1 The SEM images of the sparked NiO film: top-view at (a) low and (b) high magnifications and (c) cross-sectional-view

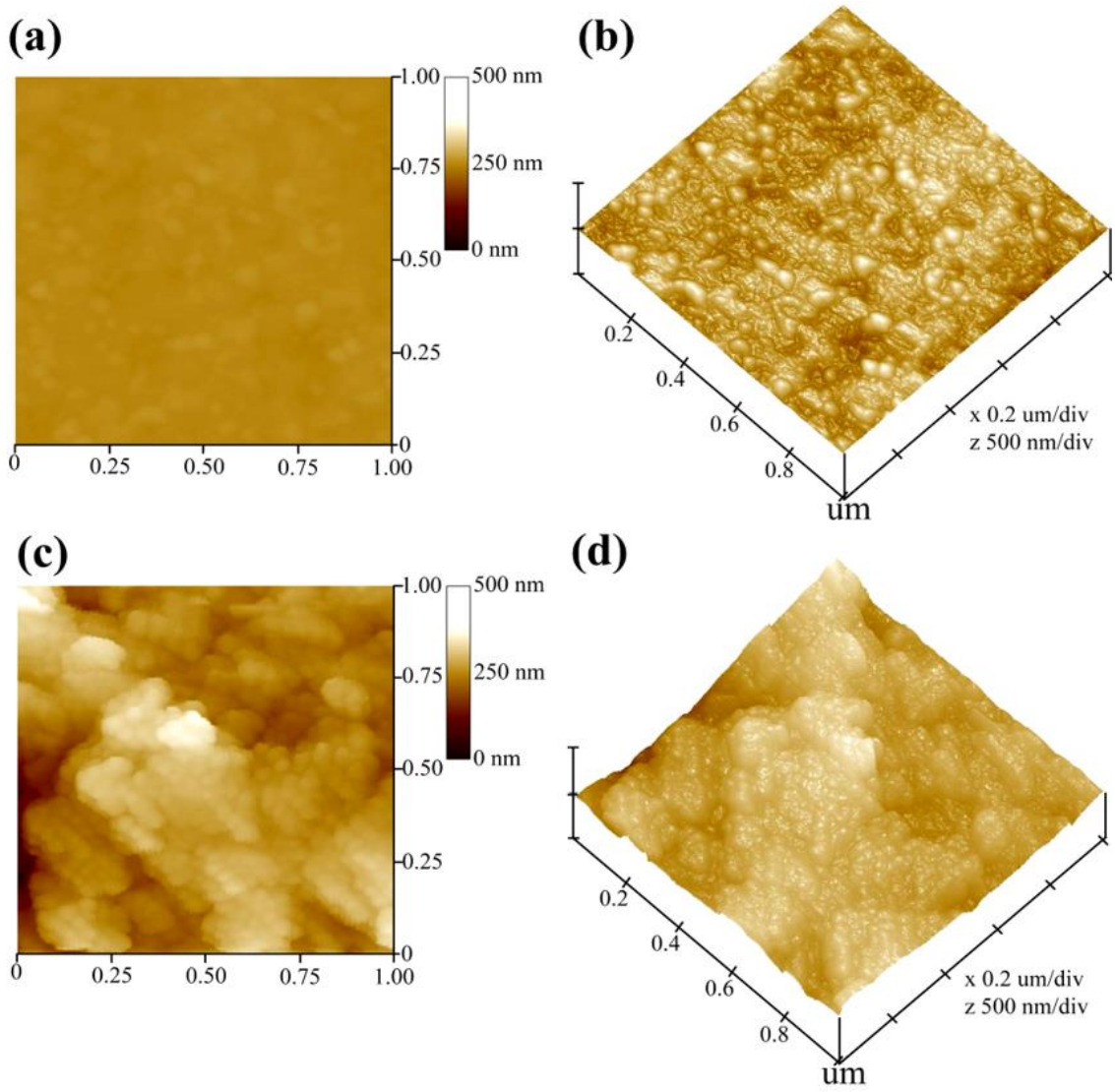

Figure 4.2 (a) 2D, (b) 3D AFM topographic images of Cr-Au on PET substrate, (c) 2D and (d) 3D AFM topographic images of NiO sparked surfaces.

nanoparticles with diameters of less than 30 nm (Figure 4.2 (c)-(d)) while the substrate is much smoother with very shallow nanoprotrusions (Figure 4.2 (a)-(b)). The result is in agreement with the SEM observations in the top area of the porous foam network (Figure 4.1 (b)). The root-mean-square (RMS) surface roughness of the substrate and NiO sparked film are determined from the AFM data to be 4.4 ± 0.4 and 40.2 ± 3.6 nm, respectively. Thus, the RMS roughness of NiO sparked film is almost 10-fold as high as that of substrate. The high RMS roughness value of the film implies a large effective surface area and high rate of the electrochemical reaction [15].

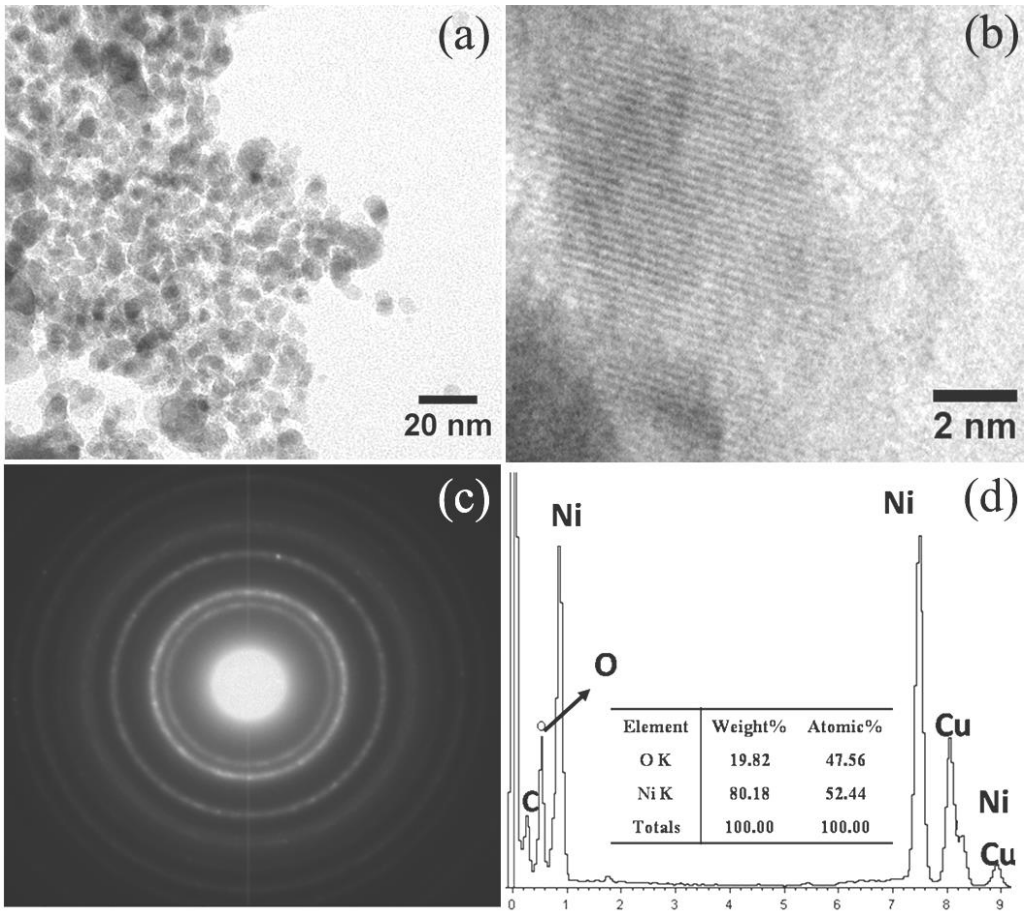

Figure 4.3 (a) TEM image, (b) HR-TEM image, (c) SAED pattern and (d) EDX spectrum of sparked NiO-NPs.

3) TEM, SAED and EDX results of the NiO nanoparticles

Figure 4.3 (a) displays a typical TEM image of NiO-NPs. It shows fine nanoparticles with uniform diameters randomly scattered on the surface. The corresponding HR-TEM image in Figure 4.3 (b) reveals that the nanoparticles are mostly spheroidal with varying diameters in the range of 3.0-6.0 nm. The results indicate that the sparking technique produces homogeneous nanoparticles with narrow particle size distribution. In addition, lattice fringes can be observed on some nanoparticles with the inter planar distance of ~0.21 nm, which is corresponding to the d-spacing on (200) of cubic NiO [181, 182]. The corresponding SAED pattern of NiO-NPs is shown in Figure 4.3 (c). It demonstrates ring diffraction patterns, identifying that the NiO particles have a polycrystalline structure. From indexing the diffraction pattern, the four main diffraction rings are found to closely match with the (111), (200), (220), and (311) planes of the cubic NiO phase (JCPDS 78-0429) [27]. Thus, as-produced

sparked powders are confirmed to be NiO nanoparticles with polycrystalline structure. Figure 4.3 (d) illustrates a typical EDS spectrum of the NiO-NPs on a carbon/copper TEM grid. It confirms all expected elements, including nickel (Ni), oxygen (O), copper (Cu) and carbon (C) of the nanoparticles and TEM grid. By excluding the elements from the grid, the atomic percentages of O and Ni are determined to be 47.6% and 52.4%, respectively. The composition is close to the ideal stoichiometric NiO.

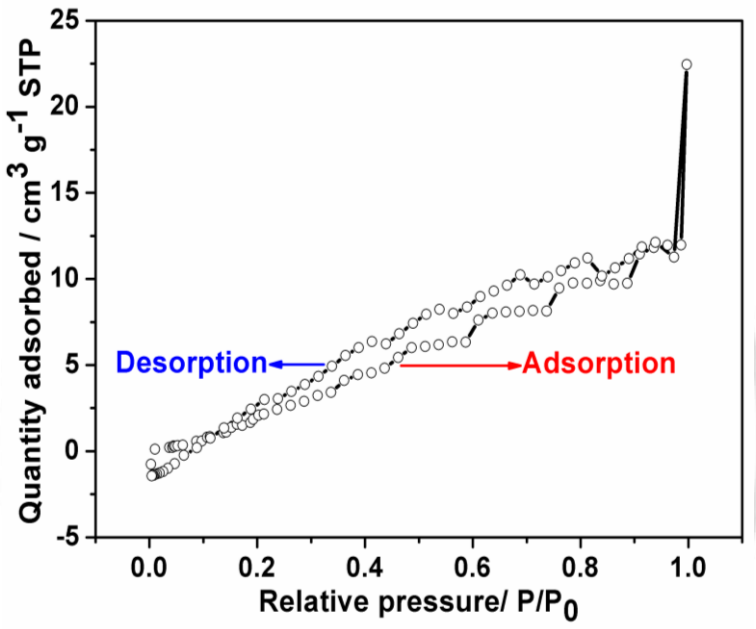

Figure 4.4 Nitrogen adsorption and desorption isotherms of NiO film

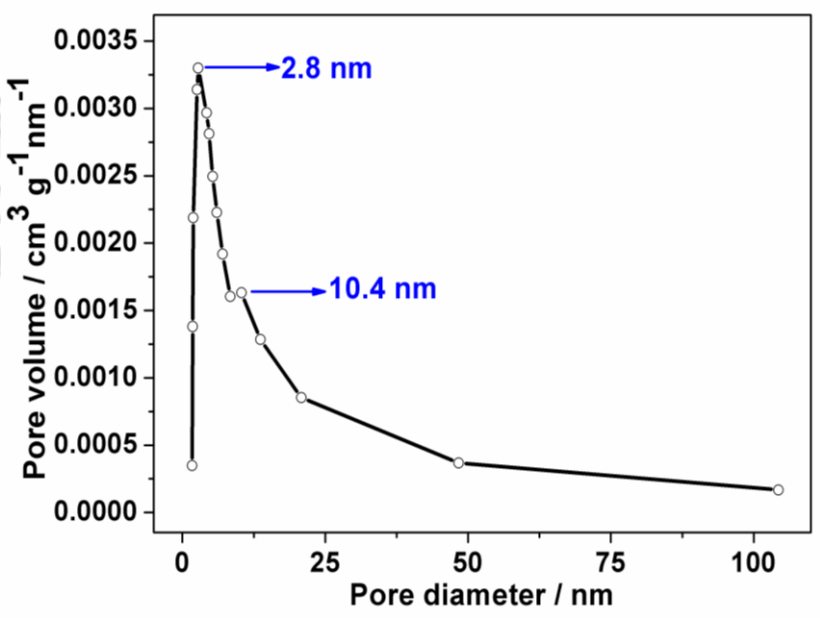

Figure 4.5 The corresponding BJH pore size distribution of NiO film

4) BET results of the NiO films sparked on flexible Cr/Au coated PET substrates

Fig 4.4 displays the N2 adsorption-desorption isotherm of sparked NiO film. It can be seen that the film shows type VI pattern according to IUPAC classification[183, 184], corresponding to a stepwise multilayer adsorption process, which occurs due to a multimodal pore distribution. The estimated BET surface area from the adsorption data is ~16 m^2g^{-1}, which is considered a high value for a thin film structure. The calculated BJH pore size distribution of the NiO film (Figure 4.5) demonstrates two maximum pore sizes at ~2.8 and ~10.4 nm, indicating the mesoporous structure. The high film porosity will provide an efficient transport pathway for ions to the interior of the sample, which is beneficial for electron transfer and adsorption, leading to a high charge capacity.

5) XRD results of the NiO films sparked on flexible Cr/Au coated PET substrates

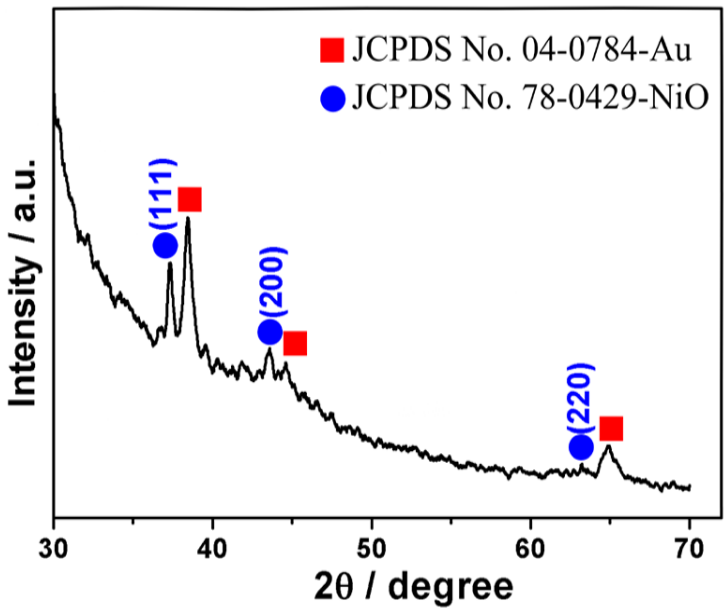

Figure 4.6 GIXRD pattern of sparked NiO film on Au/Cr coated PET substrate.

The GIXRD pattern of as-deposited NiO films on Au/Cr coated PET substrates is shown in Figure 4.6 (a). It is seen that the diffraction peaks can match well with the polycrystalline cubic NiO (JCPDS: 78-0429) and gold (JCPDS: 04-0784). For NiO, the diffraction on (111) plane is only clearly visible white diffractions on (200) and (220) are very weak and almost the same as background noise. The result is due to

the fact that the GIXRD technique is not very sensitive to plane perpendicular to the film surface. Nevertheless, this method allows a significant reduction of diffraction from the Au film on PET substrate. It can also be noticed that there is a significant background slope at low diffraction angles due to the effect of amorphous PET substrate. In addition, it is observed that the NiO peaks appear to be quite narrow, implying quite large crystallite size of NiO nanoparticles in the film, which is in contrast to the observed nanoparticle size determined by TEM of 3-6 nm. The paradox could be due to the fact that diffraction signal of NiO is not much larger compared with that background noise so that the peak shape and related crystallite size are highly uncertain. Thus, GIXRD only allows the confirmation of NiO phase in the film while the actual crystallite size of NiO nanoparticles in the film cannot yet be determined but it can be implied that the value should be smaller than the size of TEM primary particles.

6) Uv-vis results of the NiO films sparked on flexible Cr/Au coated PET substrates

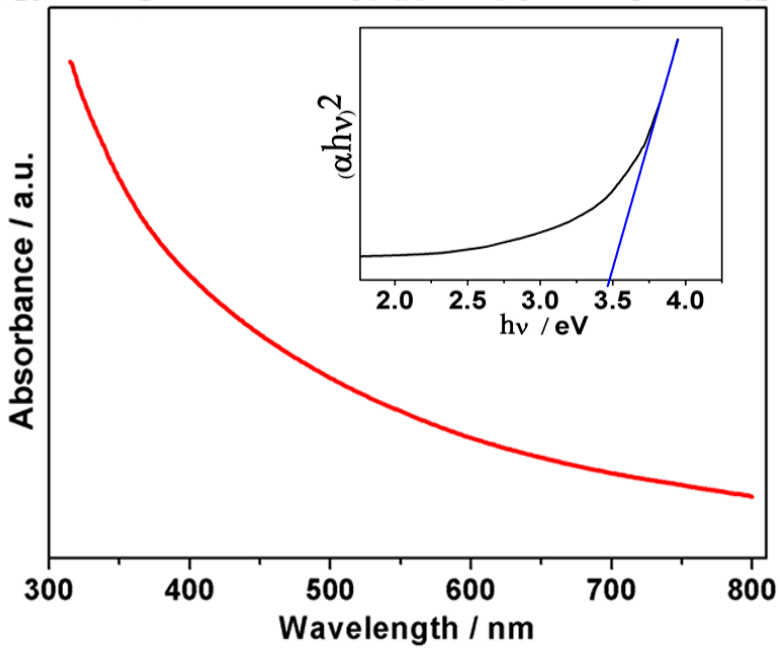

Figure 4.7 UV-vis spectrum (Inset: plot of $(\alpha h\nu)^2$ vs. $h\nu$).

Figure 4.7 (b) illustrates a typical UV-vis spectrum of sparked NiO-NPs on glass substrate. It is seen that NiO-NPs exhibit strong absorption in the near-UV region, which can mainly be attributed to the band gap absorption [185]. The value of

the band gap (E_g) can be calculated based on the fundamental absorption equation, which is given by equation 4.1 [186]:

$$\alpha h\nu = A(h\nu - Eg)^n \quad (4.1)$$

where α is the absorption coefficient, E_g is the energy band gap, hν is photon energy, A is a constant relative to the materials and n is a characteristic number, 1/2 and 2 for direct and indirect band gap transitions, respectively. For NiO, n = 1/2 since it is a direct band gap semiconductor. The inset graph presents the plots of $(\alpha h\nu)^2$ as a function of hν. It is seen that the plot (black curve) is linear only in the high energy region (> 3.6 eV) where fundamental band gap absorption occurs. The absorption at lower energy comes from other process such as absorption via defect states and thus does not conform to equation (4.1). E_g of NiO-NPs is estimated to be around 3.47 eV by extrapolation of the linear region to the energy intercept (blue line). The value is in accordance with the value of NiO nanostructures in literature [187, 188] and thus confirms the formation of NiO nanoparticles.

7) XPS results of the NiO films sparked on flexible Cr/Au coated PET substrates

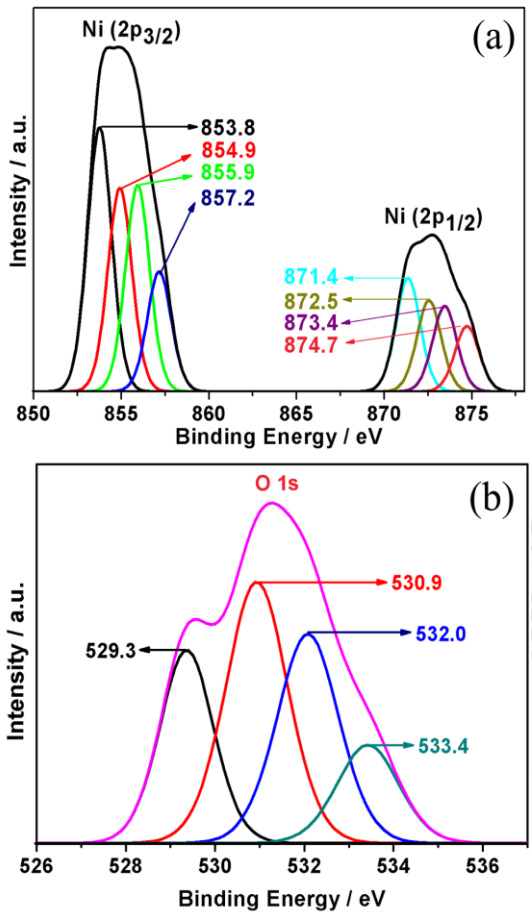

Figure 4.8 (a) Ni 2p and (b) O 1s XPS spectra of sparked NiO film

The surface compositions and chemical states of sparks NiO are further confirmed by using XPS. Figure 4.8 (a) shows the Ni 2p core levels of sparked NiO-NPs. The core levels, Ni $2p_{3/2}$ and Ni $2p_{1/2}$, can be deconvoluted in to four doublet pairs at ~853.8:871.4, ~854.9:872.5, ~855.9:873.4 and ~857.2:874.7 eV, respectively. These doublet peaks may be assigned to Ni^{2+} of NiO, Ni^{2+} of $Ni(OH)_2$, Ni^{3+} of Ni_2O_3 and Ni^{3+} of NiOOH, respectively [189-191]. For the oxygen element (Figure 4.8 (b)), the O 1s core level spectrum can be similarly decomposed into four components located at ~529.3, ~530.9, ~532.0 and ~533.4 eV, respectively. The peak at 529.3 corresponds to the lattice oxygen of NiO while the ones at ~530.9, 532 and 533.4 eV can be assigned to adsorbed oxygen species, adsorbed OH^- group due to humidity [2, 192, 193] and adsorbed -C-O- groups due to hydrocarbon impurities [194]. The results indicate that NiO-NPs formed by sparking method are complex nickel oxide.

4.1.2 Electrochemical characteristics of the NiO films sparked on flexible Cr/Au coated PET substrates

1) CV results of the NiO films sparked on flexible Cr/Au coated PET substrates

The electrochemical characteristics of the sparked NiO film studied using CV and GCD are illustrated in Figure 4.9. Figure 4.9 (a) shows a comparison of the CV curves in the potential window of 0 to 0.45 V (vs. Ag/AgCl) of the Cr-Au electrode on PET substrate with and without the sparked NiO films. It is evident that only NiO films exhibits high and sharp redox peaks, indicating its highly effective faradaic nature[195]. In contrast, the Cr-Au electrode on the PET substrate gives very low signal current and negligible peak. Thus, the NiO film will contribute almost all of charge storage capacity from the structure. The anodic and cathodic peaks at ~0.41 and ~0.32 V can be attributed to the redox reactions between NiO film and KOH electrolyte, in which NiOOH is oxidized to NiO and NiO is reduced to NiOOH, respectively. The reversible reaction is given by [192];

$$NiO + OH^- \leftrightarrow NiOOH + e^- \quad (4.2)$$

According to the XPS data, $Ni(OH)_2$ is also formed at the electrode surface. Thus, $Ni(OH)_2$ may also be reversibly converted to NiOOH according the redox reaction[196, 197];

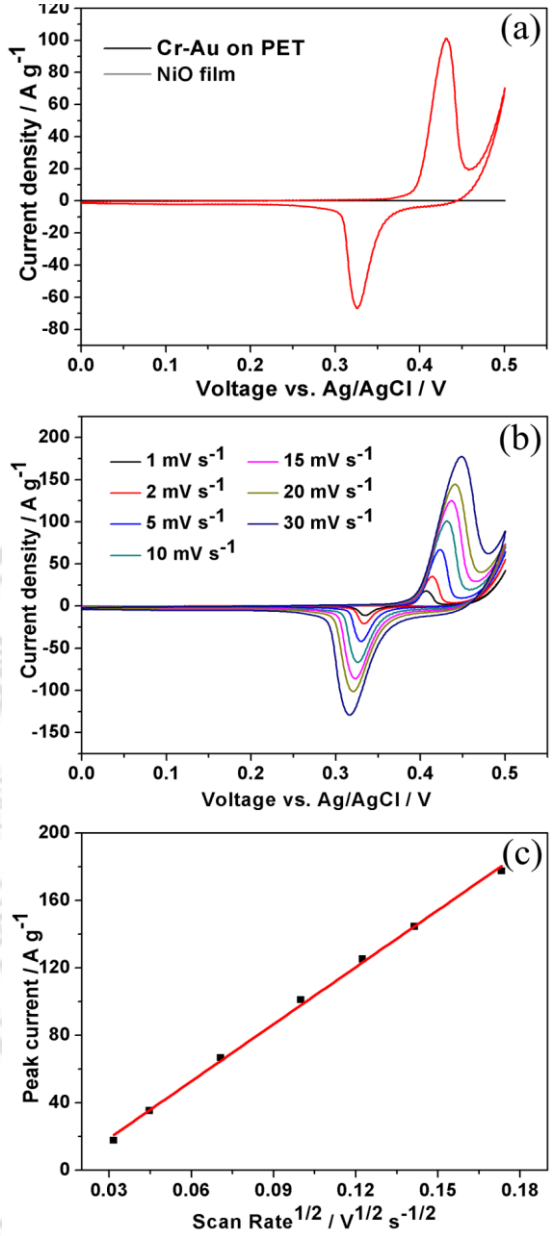

Figure 4.9 (a) CV curve of the Cr-Au on PET substrate vs. sparked NiO film at a scan rate of 10 mV s-1, (b) CV graph of NiO film at different scan rates and (c) oxidation peak current vs. square root of scan rate of sparked NiO film.

$$Ni(OH)_2 + OH^- \leftrightarrow NiOOH + H_2O + e^- \quad (4.3)$$

Figure 4.9 (b) illustrates the CV profiles of the NiO film at different scan rates. It is seen that the CV peak current density increases monotonically with increasing scan rate, suggesting a good rate capability of the NiO films. In addition, the redox peak potential also increases accordingly with increasing scan rate. Figure 4.9 (c) shows the plot of the oxidation peak current vs. square root of scan rate. It is evident that the

oxidation peak current is linearly proportional to the square root of scan rate, indicating that the redox reaction at NiO electrode is diffusion limited [198]. The characteristic is different from a typical capacitive behavior, in which peak current is proportional to the scan rate.

2) GCD results of the NiO films sparked on flexible Cr/Au coated PET substrates

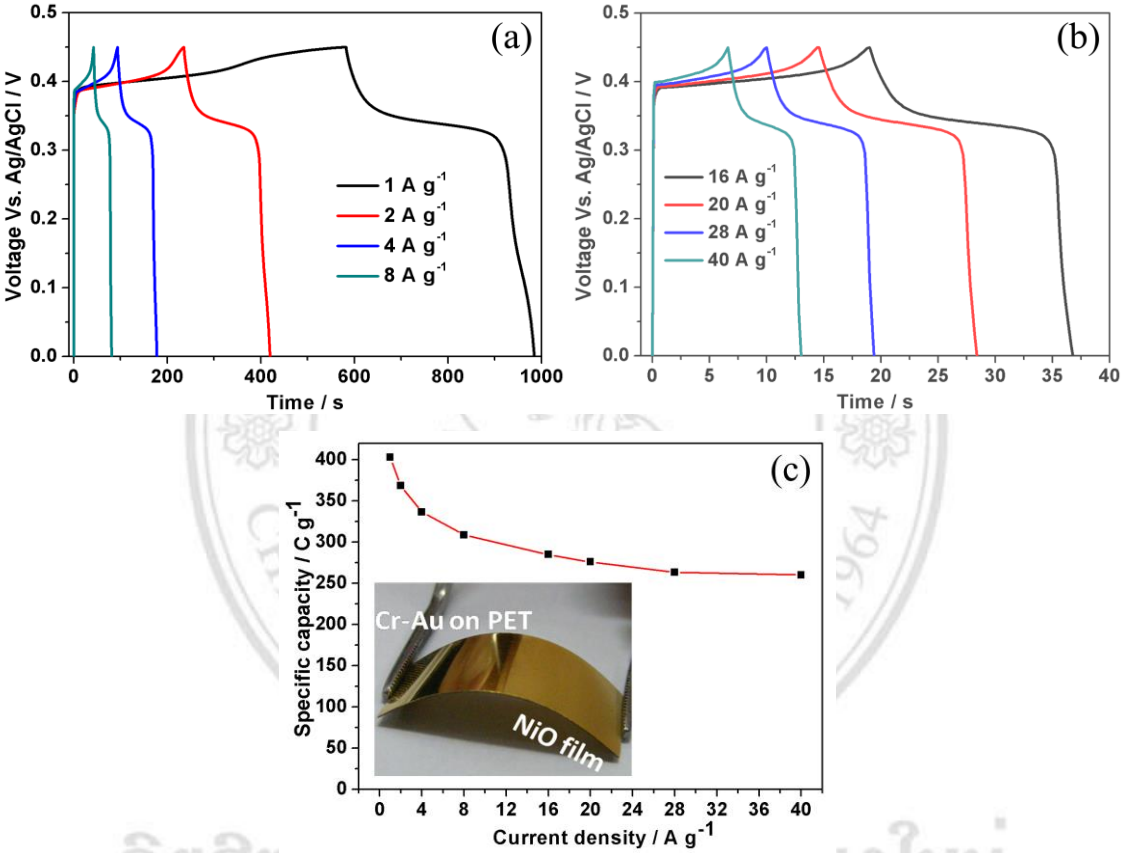

Figure 4.10 (a-b) GCD data of NiO films at low and high ranges of discharge current density, (c) specific capacity curves at a variety of current densities (Inset: photograph of bent electrode before testing).

The energy-storage characteristic of NiO electrode is then evaluated by GCD technique. Figure 4.10 (a)-(b) displays GCD curves of NiO films at low and high ranges of discharge current density, respectively. It can be seen that all discharge curves consist of three regions with initial short fast discharge (0.45-0.4 V) followed by a long and slow discharge region (0.4-0.3 V) and final rapid discharge section (0.3-0 V), which is consistent with a typical characteristic of battery-like energy-storage device and in accordance with the faradaic CV behavior. The long discharge region

corresponds to the potential at which redox peaks occur in the CV curve when the accumulated charges from redox reactions are released. Due to its battery-like characteristics, the performance of the sparked NiO electrode should be expressed in term of specific charge capacity (or in short specific capacity), which can be estimated from the GCD profile according to the defining equation:

$$\text{Specific charge capacity} = \frac{It}{m} \tag{4.4}$$

where I = discharge current, t = discharge time and m = mass of electrode material. From calculation, the sparked NiO electrode has the specific capacity values of 402.75, 368.55, 336.6, 308.7, 284.85, 275.85, 263.25 and 260.1 C g-1 at 1, 2, 4, 8, 16, 20, 28 and 40 A g^{-1}, respectively.

The specific charge capacity is plotted as a function of current density as displayed in Figure 4.10 (c). It is evident that the specific capacity rapidly decreases as the current density increases from 1 to 8 A g^{-1} but then becomes very slow decreasing as the current density increases further from 8 to 40 A g^{-1}.

Moreover, the cycling performances of sparked NiO films at 40 A g-1 is demonstrated in Figure 4.11 (a) and (b). It can be seen that NiO electrode shows highly repeatable charging/discharging profile in the first 10 cycles (Figure 4.11 (a)). Furthermore, it has a good cycling ability with a good specific capacity retention of 88 % for 1000 cycles of operation at the highest current density of 40 A g-1 (Figure 4.11 (e)). It is seen that the loss of capacity occurs mostly during first 300 cycles and the loss becomes much less as the number of cycles increases further up to 1000. The initial loss of capacity may be due to the agglomeration of the NiO particles [27] [199] or structural change of NiO nanoparticles. This problem may be alleviated by appropriate post-deposition annealing of NiO film on the Au/PET substrate. Nevertheless, the sparked NiO film can maintain 88% of initial capacity up to 1000 cycles, which is still comparable with some other reports from porous NiO on Ni foam[27].

In most reports on NiO-based electrochemical energy-storage devices, the performances were reported in term of specific capacitance instead of specific capacity due to the misconception of psuedocapacitor for nickel or cobalt oxide and

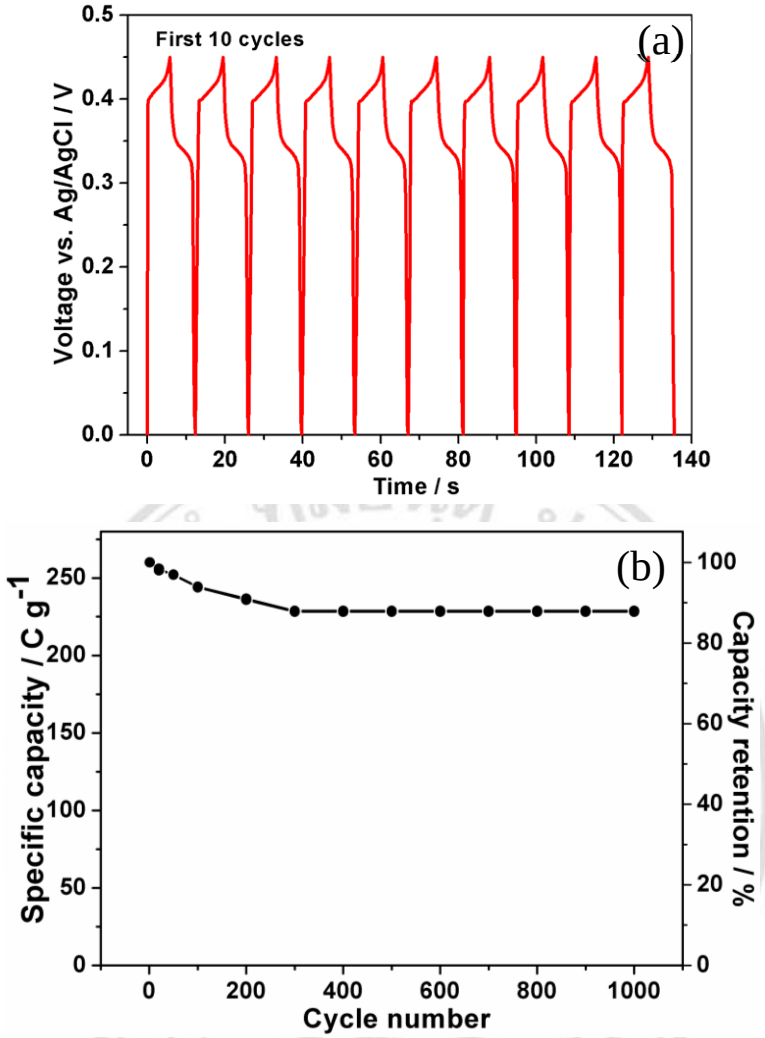

Figure 4.11 (a) GCD profiles of repeated 10 cycles at 40 A g^{-1} and (b) cycling performance of sparked NiO films at 40 A g^{-1}.

hydroxide [13]. To compare the results with other reports, the average specific capacitance is converted from the specific capacity by dividing with the potential window used in this study of 0.45 V. The average specific capacitance values of sparked NiO electrode are calculated to be 895, 819, 748, 686, 633, 613, 585 and 578 F g^{-1} (or 33.6, 30.7, 29.1, 28.0, 27.1, 25.7, 25.0, 24.4, 23.7, 23.4, 23.0, 22.0 and 21.7 mF cm-2) at 1, 2, 4, 8, 16, 20, 28 and 40 A g^{-1}, respectively. The values are comparable with some NiO-based devices, NiO nanoflowers, nanoslices and nanoparticles [2], NiO flake-like and hierarchical porous ball-like [141], porous thin film NiO nanowires [200], mesoporous NiO nanoflake arrays [201] and NiO flower-like microspheres [199], which report the specific capacitance in the range of 500-2000 F g^{-1} or 1-50 mF cm^{-2} at similar current densities. It should be noted that some work reported very high specific

capacitance value but with narrower potential window or lower current density. Moreover, a preliminary mechanical durability test was performed. The electrochemical characteristics and specific capacity of sparked NiO film were not changed considerably after a typical rolling process. In addition, no physical delamination or damage of sparked NiO film was observed. Thus, the sparked NiO film could have sufficient mechanical stability for capacitor fabrication process.

The excellent electrochemical energy-storage performances of sparks NiO film may be attributed to large specific surface area of NiO NPs for redox reactions and charge storage. In addition, the porous structure of NiO films produced by sparking process assists the transportation of ions/electrons between electrode and electrolyte and reduce ion transfer resistance to the electrodes, which could result in a low effective series resistance [202]. The sparking technique can produce more porous structure compared with several other chemical methods since no binder is included, leading to the fully accessible surface area of NiO-NPs for electrochemical reaction. Thus, the sparked NiO film is considered to be an attractive choice for electrochemical energy-storage applications due to low cost, simplicity and high charge capacity.

4.2 Results and discussion of the NiO film on Ni foams

4.2.1 Structural characterization

1) SEM results of NiO film on Ni foam

Figure 4.12 displays the surface morphologies of NiO nanostructures on Ni foams with different sparking times ranging from 45 to 180 min compared with that of a bare Ni foam. It is seen that the Ni foam has large pores whose dimensions are in the range of 100-300 μm and relatively thin lamellae whose widths are varying between 30 and 80 μm. The inset high-magnification image of a bare Ni foam shows a smooth polycrystalline surface having domain size of around few microns (Figure 4.12 (a)). After NiO sparking for 45 min, the surface becomes porous and fluffy due to the presence of very fine nanometer-sized particles along with some small voids and cavities (Figure 4.12 (b)). The particles are so small that their boundaries cannot be clearly resolved by SEM. When the sparking time increases to 90 min, it can be observed that particles begin to agglomerate into larger cluster leaving some deeper cavities (Figure 4.12 (c)). At a longer sparking time of 135 min, nanoparticles clearly

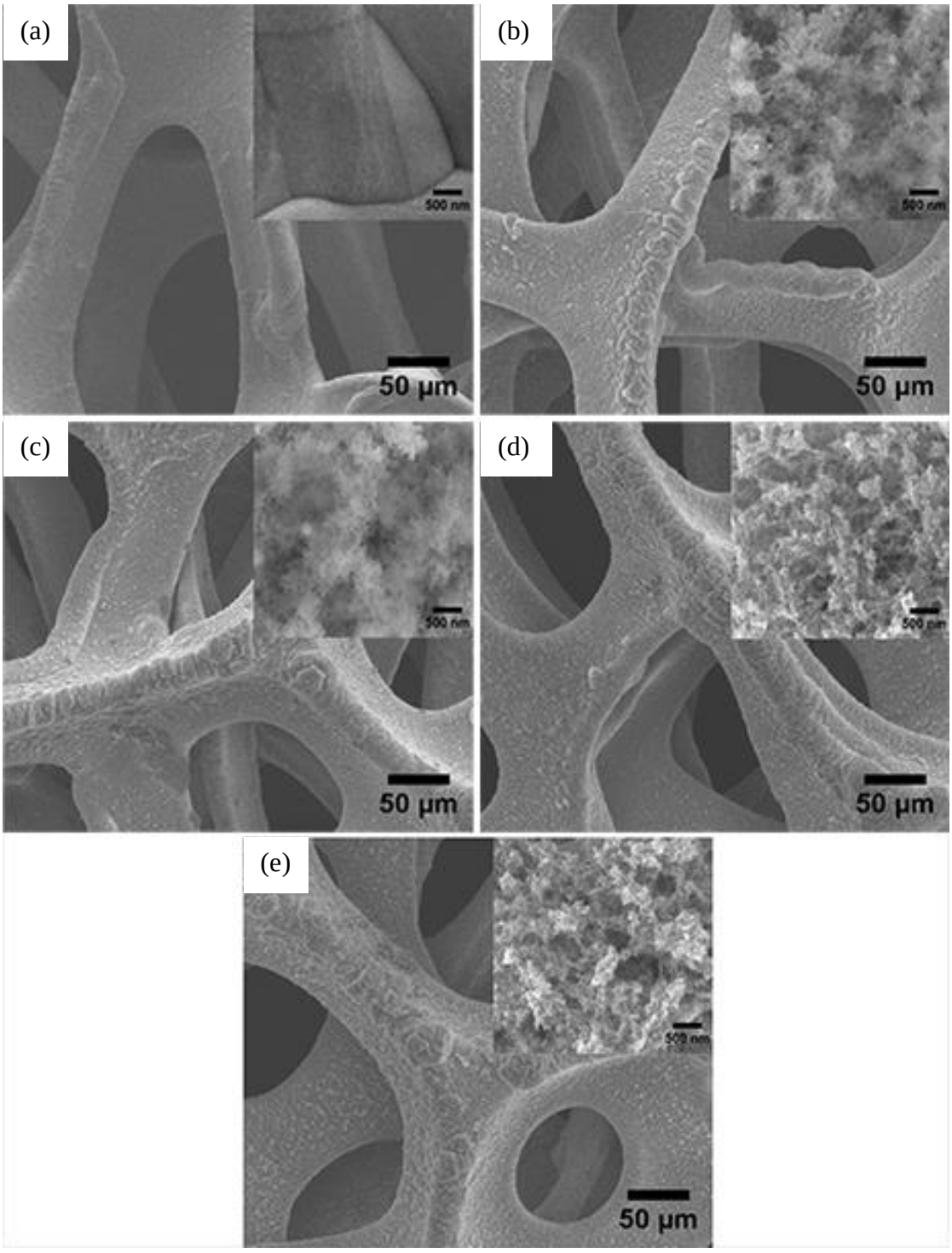

Figure. 4.12 SEM images of (a) Ni foam, (b) NiO-45min, (c) NiO-90min, (d) NiO-135min and (e) NiO-180min.

aggregate into a number of clusters with a few hundred nanometer in size that are loosely connected into a foam-like network having a number of pores with sizes ranging from a few to several hundreds of nanometers. With the longest sparking time of 180 min, the clusters grow in size and number while the cavities become relative small,

suggesting the densification of particulate network at very long sparking time. From the observations, the morphology of sparked NiO structure on Ni foam depends considerably on the sparking time. Initially, nanoporous fluffy films of NiO nanoparticles are formed at a short sparking time (45 min) and NiO nanoparticles will be aggregated into larger clusters loosely connected in the form of foam-like microporous network as the sparking time increases. The surface area of NiO structures should be initially high and tend to reduce due to increasing average cluster and pore sizes as the sparking time increases. The results are partly in accordance with the previous report of sparked In_2O_3 films on alumina substrates, which demonstrated a correlation between the morphologies of sparked films and the number of sparking cycles [36]. The observed effect may be explained based on the influence of sparking time on the temperature of arcing plasma. In the sparking process, arcing plasma generated through field ionization process will dissipate a part of its energy into heat, inducing elevated plasma and substrate temperatures, which will monotonically increase with increasing sparking time. The higher plasma temperature can affect the electric field and charge distributions of the plasma, leading to the redistribution of sparked NiO particles into nonuniform patterns, resulting in the formation of localized clusters at a long sparking time. In addition, the increase of underlying substrate temperature can accelerate the aggregation of primary particles into secondary particles or clusters [37].

2) EDX results of NiO film on Ni foam

The corresponding EDX spectra of NiO nanostructures on Ni foams are demonstrated in Figure 4.13. It is evident that all samples contain all expected elements including Ni and O of Ni foam and sparked NiO film. For the bare Ni foam (Figure 4.13 (a)), the small oxygen content of 10.86 at% is found and known to be attributed to the native oxide layer on Ni surface [203] With the presence of NiO layers (Figs. 4.13 (b)-(c)), the oxygen content increases rapidly from 31.66 to 49.12 at% as the sparking time increases from 45 to 90 min. The results confirm that the sparked Ni particles have been oxidized in air during sparking at a high plasma temperature of >1000°C [37]. The increasing O content can correlate with the increasing thickness of sparked NiO film since the EDX elemental information comes from both NiO layer and Ni foam substrate through the electron penetration depth of 2-3 μm at 20 kV. As the sparking time increases further from 90 to 180 min, the oxygen concentration increases

only slightly from 49.12 to 57.06 at%, indicating that the film thicknesses are comparable with or larger than the electron penetration depth so that the EDX information already mainly arises from the sparked NiO layer. However, the oxygen content values tend to be higher than that of the stoichiometric NiO (50 at%). This could be due to inaccuracy of EDX measurement or the excess oxygen in the sparked NiO materials. The actual surface elemental composition of NiO nanostructures will be verified by XPS measurements.

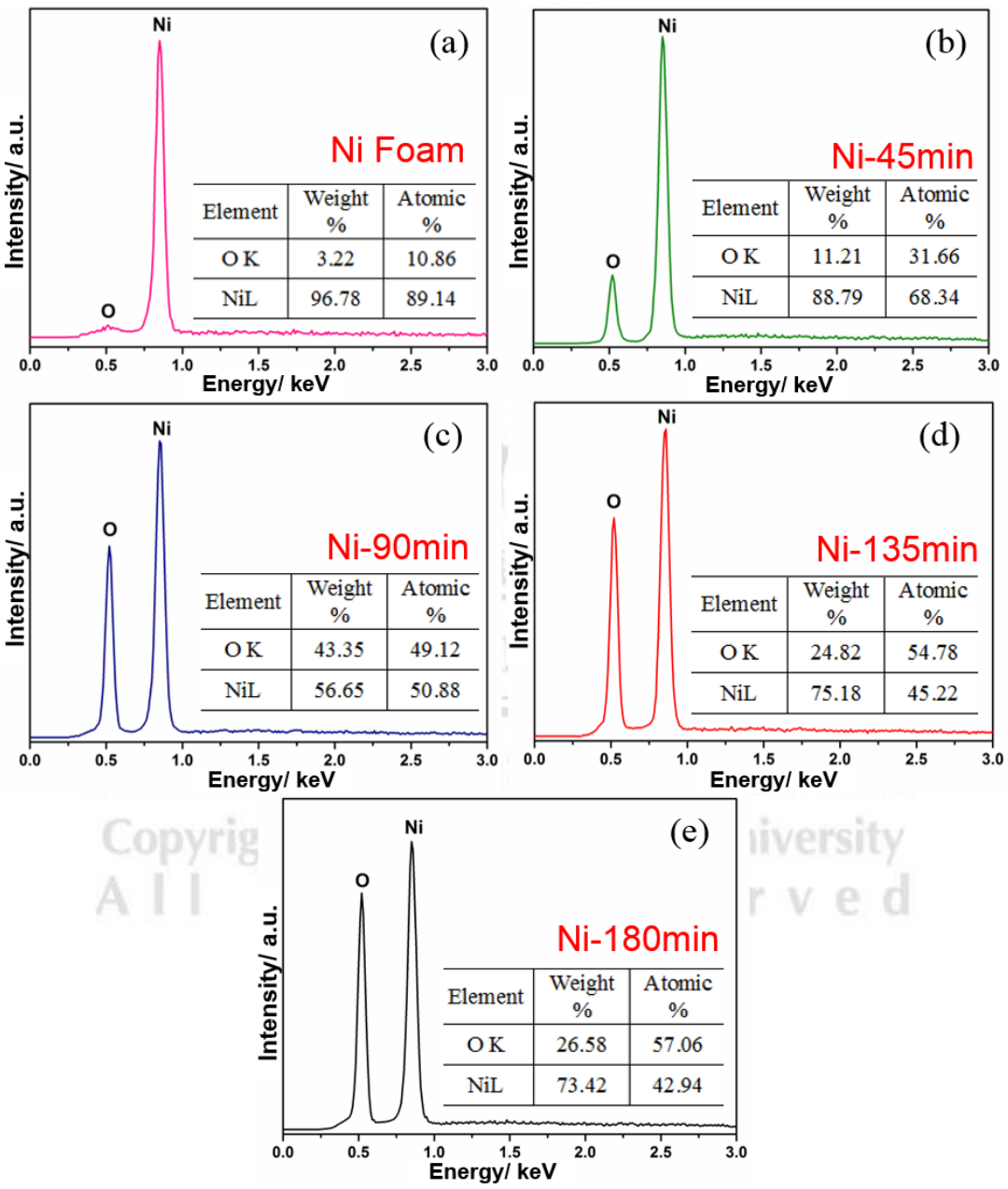

Figure. 4.13 The corresponding EDX spectra of (a) Ni foam, (b) NiO-45min, (c) NiO-90 min (d) NiO-135min, and (e) NiO-180min.

3) TEM and SAED results of NiO nanoparticles

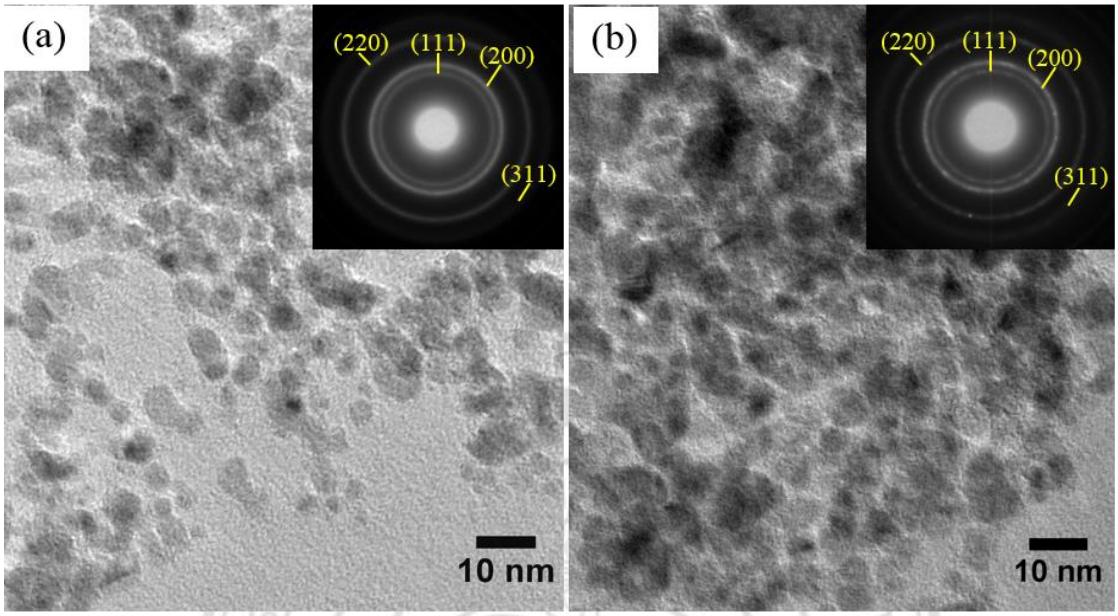

Figure. 4.14 TEM images and corresponding SAED patterns of NiO nanoparticles produced at sparking times of (a) 45 and (b) 180 min.

Figs. 4.14 (a) and (b) illustrate the TEM images of NiO nanoparticles produced at sparking times of 45 and 180 min, respectively. It is seen that the sparked NiO nanoparticles are mostly spheroidal and occasionally ellipsoidal with sub-ten nanometer dimensions. In addition, some primary NiO nanoparticles aggregate into larger secondary particles or clusters. The diameters of primary NiO nanoparticles with sparking times of 45 and 180 min are estimated to be 4.3 ± 1.7 and 7.6 ± 2.5 nm, respectively. Thus, the sparking process can produce homogeneously small NiO nanoparticles and the particle size tends to increase with increasing sparking time. This effect may also be attributed to the influence of sparking time on substrate temperature. With increasing sparking time, the substrate temperature increases accordingly, leading to the rapid growth of sparked particles. The corresponding SAED patterns of both samples (insets) display diffraction rings, which can be indexed as (111), (200), (220) and (311) planes of a cubic NiO phase (JCPDS 78-0429), confirming that the observed nanoparticles are NiO with a polycrystalline structure [27].

4) Raman results of NiO nanoparticles on Ni foam

Figure 4.15 demonstrates Raman spectra of NiO nanostructures on Ni foam deposited with different sparking times. It shows that sparked NiO structures

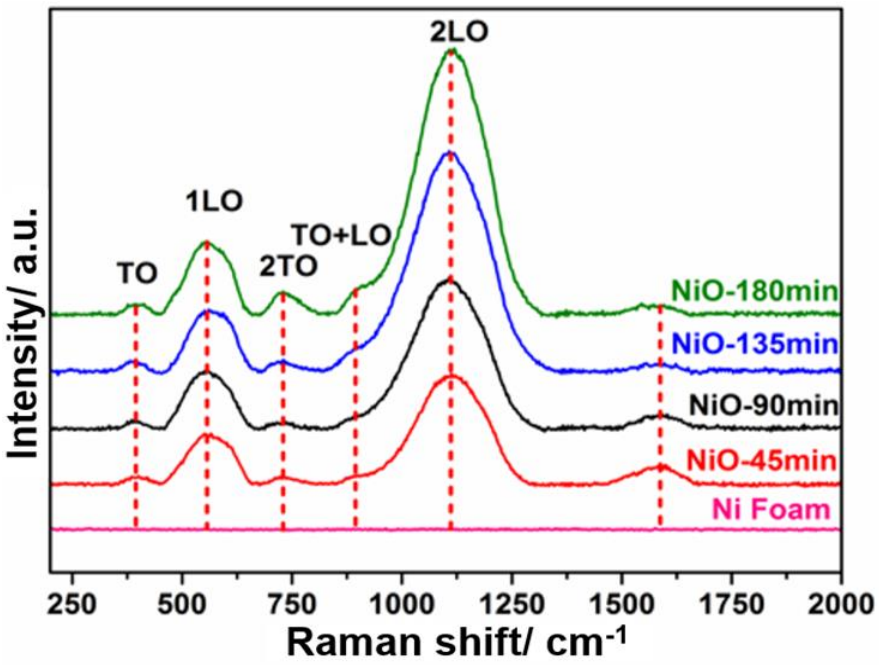

Figure 4.15 Raman spectra of sparked NiO nanoparticles on Ni foams with different sparking times.

exhibit broad Raman peaks at around 402, 559, 735, 901, 1107, and 1594 cm^{-1}, which can be assigned to 1TO (1^{st} order transverse optical phonon), 1LO (1^{st} order longitudinal optical phonon), 2TO (2^{nd} order TO), TO + LO (1^{st} order superposition) and 2LO (2^{nd} order LO) vibration modes of the cubic NiO structure [204-207]. However, the two-magnon band (2M) expected to appear in the range of 1400-1500 cm^{-1} are not found [207, 208]. In addition, there is a shallow band at 1594 cm^{-1} corresponding to amorphous carbon phase [207], which is expected to arise from some carbon impurities. Moreover, it can be observed that the Raman peak intensities of NiO films tends to become more apparent, confirming the higher amount of NiO material with increasing sparking time.

5) XPS results of NiO nanoparticles on Ni foam

Representative XPS spectra of NiO/Ni foams produced at the sparking times of 45 and 180 min are illustrated in Figure 4.16. The survey-scan XPS spectra of NiO/Ni foams (Figure 4.16 (a)) display the main XPS and Auger peaks of Ni, O and C, affirming the existence of NiO structure and some carbon contaminations. By omitting the content of carbon contamination, the surface elemental composition of NiO-45min and NiO-180min show the oxygen contents of 62.2 and 59.3 at%, respectively.

The values are considerably higher than that of the stoichiometric NiO (50 at%), suggesting the presence of nickel oxide with higher oxidation states (Ni_2O_3 or NiO_2) and/or nickel oxyhydroxide (NiOOH) on surface. For Ni element (Figure 4.16 (b)), the Ni 2p doublet pair, Ni $2p_{3/2}$: Ni $2p_{1/2}$, of NiO-45min can be deconvoluted by Gaussian fitting into three doublet pairs at the binding energies of 854.2:872.0, 855.6:873.5 and 856.9:874.9 eV while that of NiO-180min can be decomposed into four doublet components at 853.8:871.4, 854.9:872.5, 855.9:873.4 and 857.2:874.7 eV, respectively.

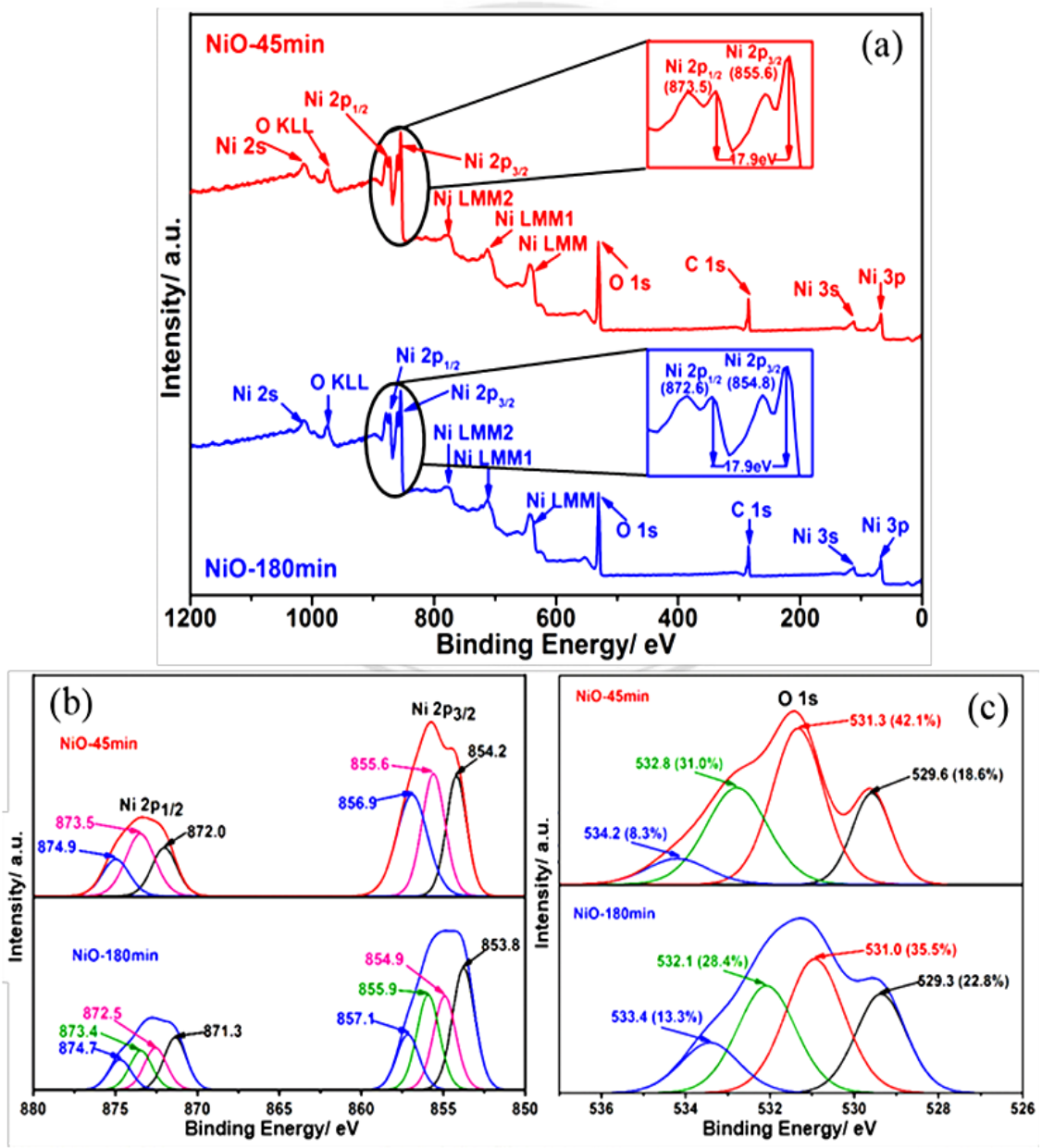

Figure 4.16 XPS spectra of NiO nanoparticles on Ni foams produced at sparking times of 45 and 180 min: (a) survey scan, (b) Ni 2p and (c) O 1s.

The energy separations (Ni $2p_{1/2}$-Ni $2p_{3/2}$) of the main Ni 2p doublet peaks (before deconvolution) for NiO-45min and NiO-180min are both equal to 17.9 eV in close agreement with most reports for NiO (17.8 eV) [209]. The peaks at 853.8–854.2, 854.9, 855.6–855.9 and 856.9–857.2 may be assigned to Ni^{2+} of NiO, mixed Ni^{2+}-Ni^{3+} of β-NiOOH, Ni^{2+} of $Ni(OH)_2$ and Ni^{3+} of α-NiOOH, respectively [189, 191]. Thus, sparked NiO structures prepared at 45 and 180 min have similar NiO/OH phase components but NiO-180min contains an additional β-NiOOH phase. In addition, it can be seen from the relative peak areas that NiO-45min comprises relatively high fraction of nickel hydroxide species.

In the case of oxygen (Figure 4.16 (c)), the O 1s peak of NiO-45 min can be decomposed into four components centered at the binding energy of 529.6, 531.3, 532.8 and 534.2 eV while those of NiO-180min are slightly shifted to 529.3, 531.0, 532.1 and 533.4 eV, respectively. They can be attributed to the lattice oxygen (O^{2-}) of NiO, chemisorbed hydroxide species (OH^-) [2, 192], adsorbed oxyhydroxide species (OOH^-) group due to humidity [210] and loosely bound oxygen species at defect sites and carbonaceous impurities [194], respectively. Moreover, the contribution of OH^- (42.1 %) and OOH^- (31.0%) for NiO-45min are notably higher than those for NiO-180min (35.5 and 28.4%) in accordance with the observed Ni species. Thus, the results indicate that the fraction of fully oxidized NiO in sparked NiO nanostructures tends to increase with increasing sparking time. This result should be due to increasing plasma and substrate temperatures, leading to the higher degree of Ni oxidation during sparking with increasing sparking time.

4.2.2 Electrochemical properties of NiO film on Ni foam

1) CVresults of NiO film on Ni foam

The CV data of sparked NiO/Ni foam electrodes with different sparking times are demonstrated in Figure 4.17. The CV curves of all NiO/Ni foam electrodes at various scan rates ranging from 5 to 50 mV s^{-1} (Figure 4.17 (a-d)) display strong anodic and cathodic peaks, indicating that the charge capacities of these electrodes mainly arise from Faradaic redox reactions at the electrode surface and the sparked NiO on Ni foam is a battery-type electrochemical energy storage electrode [29]. The redox peaks may be attributed to two reversible redox reactions of $Ni(OH)_2$/NiOOH and NiO/NiOOH according to [211-214]:

$$Ni(OH)_2 + OH^- \Longleftrightarrow NiO(OH) + H_2O + e^- \quad (4.5)$$

$$NiO + OH^- \Longleftrightarrow NiO(OH) + e^- \quad (4.6)$$

According to the XPS analysis, the $Ni(OH)_2$ content decreases with increasing sparking time. Consequently, the contribution of reaction (4.5) decreases while that of reaction (4.5) increases as the sparking time increases.

The change of these contributions may partly lead to the decreasing current density at a given scan rate with increasing sparking time as seen in Figure 4.17 (a)-(d) because the reaction rate of $Ni(OH)_2$ should be relatively high compared with that of NiO [34, 215]. Regarding the effect of scan rate on peak current, it can be observed that both of anodic and cathodic peak locations shift toward more positive and negative potentials, respectively. This behavior can be attributed to the escalating of the internal resistance of the electrode with increasing scan rate [215]. The anodic peak current is plotted with the square root of scan rate as displayed in Figure 4.17 (e). It is seen that all NiO/Ni foam electrodes exhibit linear relationships, demonstrating that the redox reactions at the sparked NiO surface is controlled by the diffusion of [OH^-] [34]. In addition, the slope of peak current vs. the square root of scan rate increases with decreasing sparking time, indicating the higher electrocatalytic activity of the NiO/Ni foam electrode prepared with a shorter sparking time [34]. The change of these contributions may partly lead to the decreasing current density at a given scan rate with increasing sparking time as seen in Figure 4.17 (a)-(d) because the reaction rate of $Ni(OH)_2$ should be relatively high compared with that of NiO [34, 215]. Regarding the effect of scan rate on peak current, it can be observed that both of anodic and cathodic peak locations shift toward more positive and negative potentials, respectively. This behavior can be attributed to the escalating of the internal resistance of the electrode with increasing scan rate [215]. The anodic peak current is plotted with the square root of scan rate as displayed in Figure 4.17 (e). It is seen that all NiO/Ni foam electrodes exhibit linear relationships, demonstrating that the redox reactions at the sparked NiO surface is controlled by the diffusion of [OH^-] [34]. In addition, the slope of peak current vs. the square root of scan rate increases with decreasing sparking time, indicating the higher electrocatalytic activity of the NiO/Ni foam electrode prepared with a shorter sparking time [34].

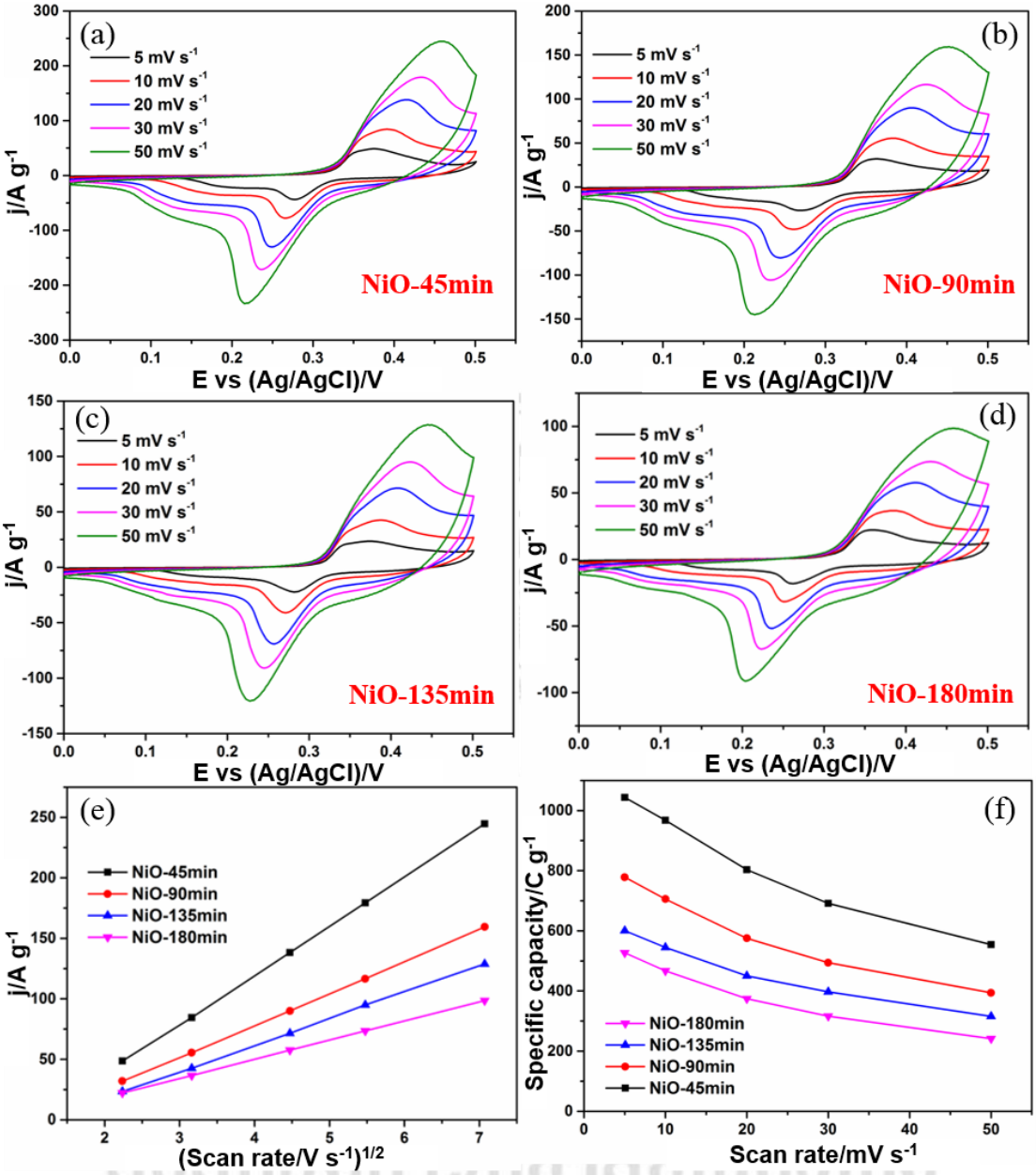

Figure 4.17 CV curves at various scan rates of NiO/Ni foam electrodes prepared with the sparking times of (a) 45 min, (b) 90 min, (c) 135 min and (d) 180 min, (e) corresponding anodic peak current vs. the square root of scan rate plots and (f) corresponding specific capacity vs. scan rate plots.

The performance of the sparked NiO on Ni foam as a battery-type electrode is characterized in term of the specific capacity (Q_{sp}, C g^{-1}) that can be calculated from CV curves according to [141, 216]:

$$Q_{sp} = \frac{1}{\nu\, m} \int_{V_i}^{V_f} i \, dV \qquad (4.7)$$

where ν is the scan rate (V s^{-1}), m is a mass of the active material (g), V_i (V) is the starting potential and V_f is the final potential (V). In addition, the average specific capacitance (C_{sp}, F g^{-1}) = $Q_{sp}\Delta V$ where $\Delta V \equiv V_f - V_i$ will also be reported here in order to allow direct comparisons with the results of several other published reports that mistakenly describe NiO and other similar materials as pseudocapacitors. Figure 4.17 (f) shows the specific capacity vs. scan rate of NiO/Ni foam electrodes prepared with various sparking times. It is seen that Q_{sp} of all electrodes decrease monotonically with increasing scan rate, signifying the lower redox activity at a higher scan rate [217]. From above analysis, the redox reactions at NiO/Ni foam electrodes are diffusion-limited. Thus, the interfacial reaction kinetics are quite slow so that ionic/electronic movements in and out of NiO surfaces cannot respond the fast potential change at a higher scan rate, leading to a lower ion transfer rate, a thinner diffusion layer and lower charge capacity [218, 219].

Moreover, it is evident that the charge capacity decreases monotonically with increasing sparking time and the NiO/Ni foam electrode produced with the shortest sparking time of 45 min exhibits the best charge storage performances with the highest and the lowest Q_{sp} (C_{sp}) values of ~1043 C g^{-1} (2087 F g^{-1}) at 5 mV s^{-1} and ~554 C g^{-1} (1109 F g^{-1}) at 50 mV s^{-1}, respectively. The effect can be explained based on the structural change observed by SEM and TEM that NiO nanoparticles become larger and aggregate into larger clusters loosely connected as a foam-like network with a large pore size as the sparking time increases, leading to a lower surface area for reactions with the alkaline electrolyte and a lower amount of charges generated through the redox reactions [3]. In addition, the NiO/Ni foam prepared at a shorter sparking time has higher contribution of more active $Ni(OH)_2$ species on surface (according to XPS data), resulting in further enhancement of faradaic reaction rates. Thus, the sparking time should be moderately short to optimize the porosity and chemical properties of sparked NiO layers on Ni foams. However, too short sparking time will lead to an incomplete coverage of NiO layer on Ni foam and a lower charge capacity. It has been found that 45 min is the shortest time that yields sufficiently complete NiO coverage on Ni foam and it is thus selected as the minimum sparking time. Moreover, the attained charge capacity (1043 C g^{-1} @5 mV s^{-1}) of the optimal electrode (NiO-45min) is considerably better than other previously reported NiO-based electrodes having various morphologies

prepared by different methods as listed in Table 4.1, which offered Q_{sp} values in the range of 162-548 C g^{-1} @1-5mV s^{-1} [30, 220].

2) GCD results of NiO film on Ni foam

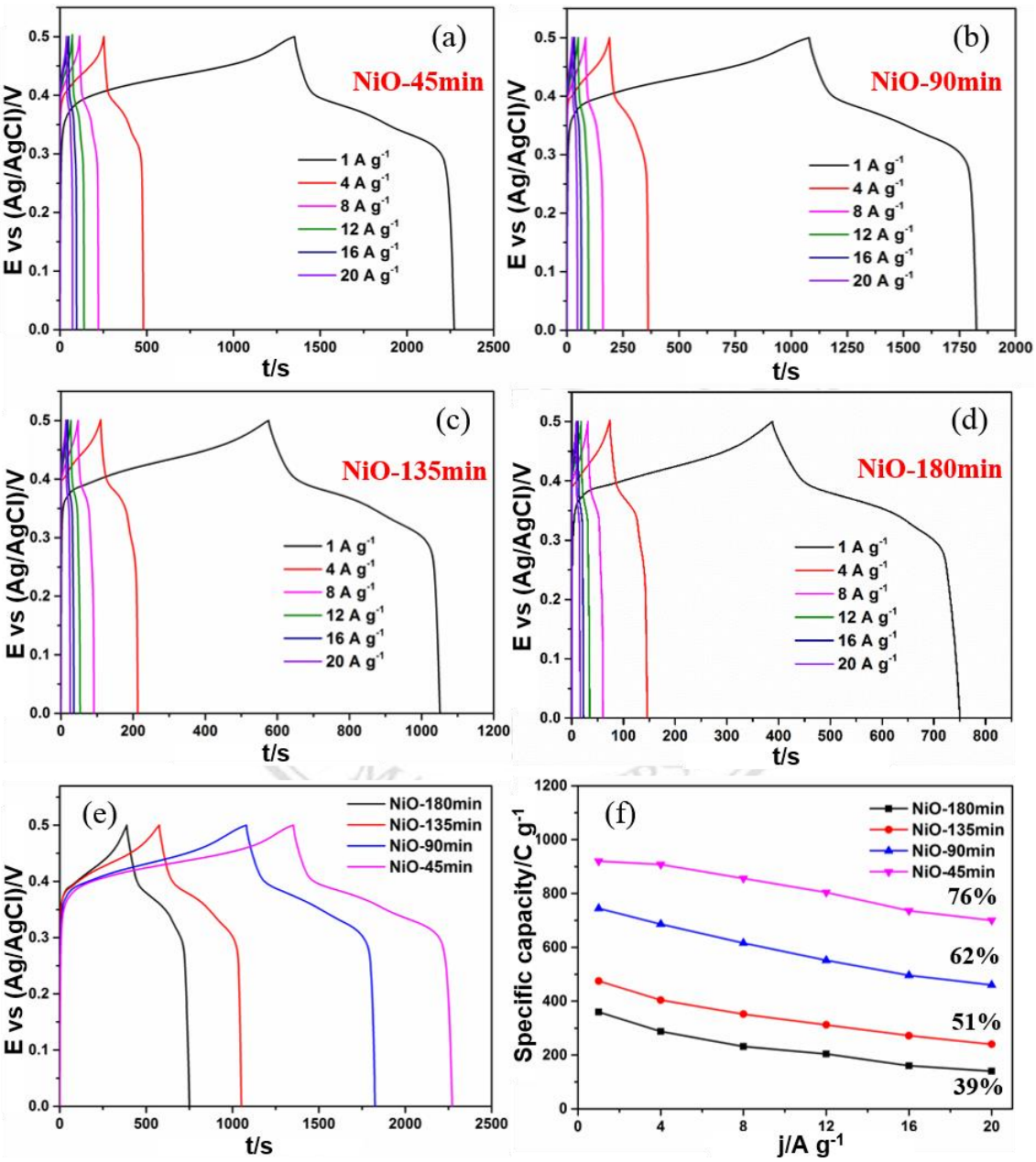

Figure 4.18 GCD curves at various current densities of NiO/Ni foam electrodes prepared with the sparking times of (a) 45 min, (b) 90 min, (c) 135 min and (d) 180 min, (e) GCD curves at a current density of 1 A g^{-1} of sparked NiO films with varying sparking times and (f) the corresponding specific capacity vs. current density.

Figure 4.18 illustrates the GCD data of NiO/Ni foam electrodes prepared with different sparking times. The NiO/Ni foam electrodes are characterized by GCD. The GCD curves at various current densities of sparked NiO films with different sparking times (Figs. 4.18 (a)-(d)) show non-linear charge-discharge behaviors, confirming a battery-type charge storage mechanism of sparked NiO structures in accordance with the CV results. In addition, the charge and discharge times decrease more rapidly with increasing current density. The discharge profiles can be divided into three distinct regions. The first region (0.5-0.38 E Vs (Ag/AgCl)/V) begins with a rapid decay of potential with time, followed by a much slower discharge regime (0.38-0.28 E Vs (Ag/AgCl)/V) and the last section (0.28-0 E Vs (Ag/AgCl)/V) having a very fast potential drop behavior. The middle regime corresponds to the region of faradaic reaction peaks that generate the majority of stored charges while the other two regions contribute very small amounts of charges due to much lower redox reactionrates. To see the effect of sparking time on GCD behaviors, the GCD curves of sparked NiO/Ni foam electrodes with various sparking times are compared at a current density of 1 A g^{-1} as displayed in Figure 4.18 (e). It is evident that the charge and discharge times decrease monotonically as the sparking time increases from 45 to 180 min, signifying the decrease of charge capacity in agreement with the CV results. The specific charge capacity, Q_{sp}, can be calculated from GCD curves according to equation 4.4.

Figure 4.18 (f) shows the specific capacity vs. current density of NiO/Ni foam electrodes with different sparking times. It is apparent that the Q_{sp} value decreases monotonically with increasing current density, similar to the decreasing trend of CV-derived Q_{sp} with increasing scan rate (Figure 4.17 (f)). In addition, the Q_{sp} values obtained from GCD are in the same range as the values calculated from CV. The amount of stored charges decreases at a higher current density because fewer ions can penetrate into the inner pore surfaces when the potential changes rapidly due to fast charging and discharging at a high current [217, 221]. At the lowest current density of 1 A g^{-1}, NiO/Ni foam electrodes prepared with sparking times of 45, 90, 135 and 180 min exhibit high specific capacities of 920 C g^{-1} (1840 F g^{-1}), 745 C g^{-1} (1490 F g^{-1}), 475 C g^{-1} (950 F g^{-1}) and 360 C g^{-1} (720 F g^{-1}), respectively. When raising the current density from 1 A g^{-1} to 20 A g^{-1}, corresponding Q_{sp} values of the electrodes reduce to 76%, 62%, 51% and 39% of their highest values at 1 A g^{-1}, respectively. Thus, the NiO-45min

electrode exhibits not only higher specific capacity but also better discharge rate capability than other NiO/Ni foam electrodes. Furthermore, the achieved GCD performances (920 C g^{-1} @1 A g^{-1} and 699 (76% of 920) C g^{-1} @20 A g^{-1}) of NiO-45min are also superior to other NiO-based electrodes as summarized previously in Table 4.1, which offered Q_{sp} values in the range of 129-755 C g^{-1} @0.1-1 A g^{-1} [222, 223]. The efficacy of NiO/Ni foam electrode with the short sparking time of 45 min may be attributed to binder-free nanoporous morphology with very small particle and pore sizes as well as a low degree of agglomeration of NiO nanostructures, enhancing the faradaic process particularly the transportation and diffusion of ions/electrons between the active material and the alkaline electrolyte [202]. Moreover, the results are also substantially higher than the NiO nanoparticles sparked on planar Au/PET substrates (403 C g^{-1} @1 A g^{-1}) [35], demonstrating that 3D Ni foam substrates can significantly enhance the surface area of sparked NiO nanostructures.

Figure. 4.19 (a) illustrate the GDD profiles of NiO-45min and NiO-180min for 10 cycles of charging/discharging at 4 A g^{-1}. It is seen that both NiO/Ni foam electrodes display repeatable charging/discharging profiles in these 10 cycles. The corresponding specific charge capacity was calculated from the GCD profiles and plotted as a function of the cycle number up to 1000 as shown in Figure 4.19 (b). From the results, the charge capacities of NiO-45min and NiO-180min increase gradually as the number of cycles rises from 0 to 100-150 up to ~110% and 103% of their starting values, respectively. This behavior may be attributed to the enhancement of surface wettability after the initial cycles via cycle induction [228], leading to higher electro-active NiO surface area for redox reactions [229].

As the cycle number increases further, the capacities of both electrodes decrease slowly and become quite steady at a large number of cycles (>900). At 1000 cycles, the NiO-45min and NiO-180min can retain ~96% and ~89% of specific capacities relative to their initial values. The better cycling performances of NiO-45 min electrode may be related to the superior adhesion of thin sparked NiO layer on Ni foam compared with that of thicker one. From structural characterizations, the thicker sparked NiO layer contains more loosely agglomerated NiO nanoparticles with larger particle and pore sizes, which may be more easily detached from the structure by vigorous redox reaction leading to higher loss of capacity. The obtained cycling performances are better than or

comparable with several other reports except a few as listed in Table 4.1. Therefore, the NiO/Ni foam electrode prepared by sparking method is highly attractive for electrochemical energy-storage applications because of its excellent charge capacity, rate capability and cycling performances as well as low cost, environmental friendly and simple fabrication process.

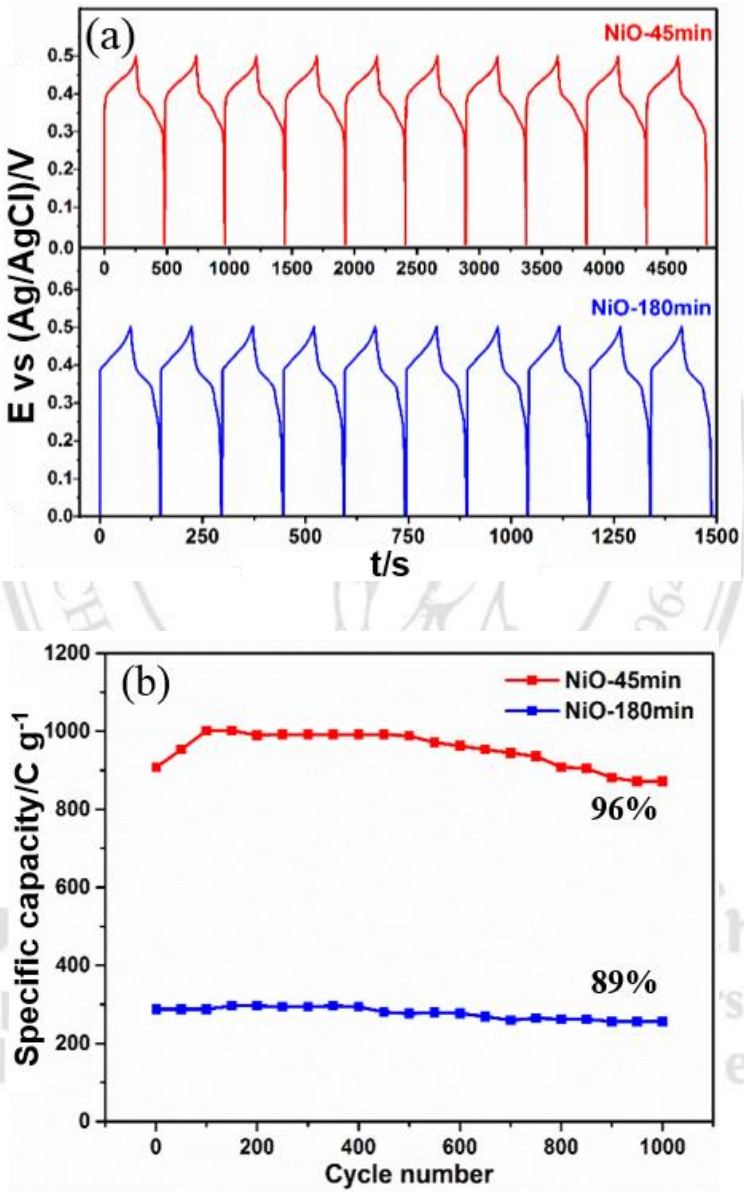

Figure 4.19 (a) The first 10 cycles of GCD profiles at 4 A g^{-1} of NiO-45min and NiO-180min and (b) the corresponding cycling performance of specific capacity at 4 A g^{-1} up to 1000 cycles.

Table 4.1 Charge storage performances of NiO-based electrodes prepared by various methods.

Materials	Methods	Q_{sp} (C g^{-1})	Cycling performance	Ref.
NiO thin film	Spray deposited	162@5mV s^{-1}	92.1%@1A g^{-1}, 1000 cycles	[30]
NiO thin film	Chemical precipitation	200.4@20mV s^{-1}	Not report	[31]
NiO Nanotubes	Anodic aluminum oxide template	133@0.1A g^{-1}	93%@0.1A g^{-1}, 1000 cycles	[224]
NiO nanoflakes	Potentiodynamic deposition	133.2@0.1mA cm^{-1}	94%@100mVs^{-1} 1000 cycles	[225]
NiO hexagonal nanoplates	Surfactant self-assembly	129@1A g^{-1}	88.5%@1A g^{-1}, 1000 cycles	[222]
Hollow NiO nanofibers	Electrospinning	144.5@5 mA cm^{-1}	87%@5mAcm^{-1}, 1000 cycles	[212]
Porous NiO nanowall arrays	Direct synthesis	148.5@0.67A g^{-1}	93%@13.35A g^{-1}, 4000 cycles	[226]
NiO nanoplatelets	Microwave method	548@1 mV s^{-1}, 780@1 A g^{-1}	98.5%@2 A g^{-1}, 1000 cycles	[34]
Porous NiO microflowers	Coordination of microflowers	755.1@0.625A g^{-1}	99.7@6.25 A g^{-1}, 1000 cycles	[223]
NiO spherical spongy	Reflux	505@1 A g^{-1}	139.6%@4 A g^{-1}, 1000 cycles	[33]
NiO urchinlike	Hydrothermal	145@4mA g^{-1}	99.7%@4mA g^{-1}, 500 cycles	[227]
NiO flower-like microspheres	Hydrothermal	259@1 A g^{-1}	96%@15 A g^{-1}, 1000 cycles	[199]
NiO nanoparticles	Hydrothermal	476.3@1 A g^{-1}	62%@5 A g^{-1}, 3750 cycles	[32]
NiO nanoparticles on AU/PET sheets	Sparking method	402.7@1 A g^{-1}	88%@40 A g^{-1}, 1000 cycles	[35]
NiO nanoparticles on NiO foam	Sparking method	1043@5 mV s^{-1}, 920@1 A g^{-1}	96%@4 A g^{-1}, 1000 cycles	**This work**

3) EIS results of NiO film on Ni foam

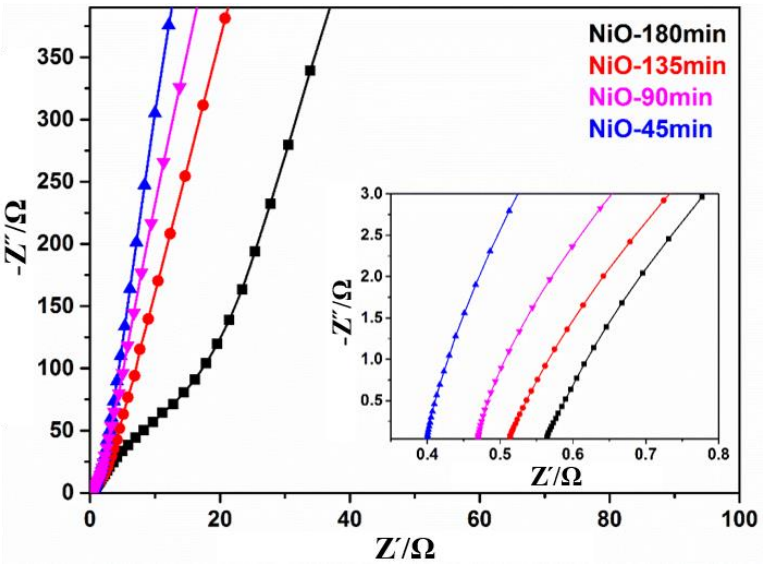

Figure 4.20 Nyquist plots of sparked NiO/Ni foam electrodes with different sparking times.

Figure 4.20 demonstrates the EIS characteristics of sparked NiO/Ni foam electrodes with various sparking times. The observed impedance behaviors of the NiO-based electrodes may be described by two distinct mechanisms taking place in low and high frequency regions. In the low frequency region, the impedance displays a steep slope of 70-75°, which may be attributed to faradaic process at the NiO/Ni foam electrode, exhibiting a non-ideal capacitive behavior [230]. For the high frequency region, the impedance exhibits a smaller slope at an angle of 50-60°, signifying the process of ion diffusion into the porous NiO/Ni foam electrodes and the higher angle may imply the higher diffusion rate and lower charge transfer resistance due to the more porous structure of sparked NiO/Ni foam at a shorter sparking time [231]. The equivalent series resistance (ESR) can be determined from the intercept to the real part (Z') of impedance at high frequency (Inset). It is clear that the ESR value of NiO/Ni foam increases monotonically from 0.40 to 0.56 Ω as the sparking time increases from 45 to 180 min. For this structure, ESR is the total equivalent resistance, comprising the internal resistance of NiO layer as well as Ni foam, the ionic resistance of the electrolyte and the contact resistance between NiO and current collector (Ni foam) [29, 231-233]. The lower ESR value at a shorter sparking time implies the lower internal resistance of sparked NiO layer, which should be due mainly to the smaller film thickness. Therefore, the superior electrochemical charge-storage properties of NiO-45min observed from the CV and GCD data can also be related to the smaller internal and charge transfer resistances of the more porous and thinner sparked NiO layer.